Supporting Information for

Carbon-cement supercapacitors as a scalable bulk energy storage solution

Nicolas Chanut, Damian Stefaniuk, James C. Weaver, Yunguang Zhu, Yang Shao-Horn, Admir Masic, Franz-Josef Ulm

Corresponding Franz-Josef Ulm.
E-mail: ulm@mit.edu

This PDF file includes:

Supporting text
Figs. S1 to S11
Tables S1 to S4
SI References

Supporting Information Text

This supporting document provides additional information on (1.) Carbon-Cement Material and Electrode Design; (2.) Texture analysis using a correlative EDS–Raman spectroscopy approach to map the carbon network for spatial correlation analysis; (3.) Derivations of the steady-state solutions for cyclic voltammetry (CV) and galvanostatic charge-discharge (GCD); and (4.) Dimensional analysis and scaling of energy storage and rate. All experimentally acquired and/or extracted results are also included in this supporting information document.

Contents

1 Carbon-Cement Materials and Electrodes **2**
A Sample Preparation . . . 2
B Carbon-Cement Electrodes and Constituent Properties . . . 3
C Microindentation . . . 4

2 Texture Analysis **4**
A Correlative High Vacuum EDS–Raman Spectroscopy . . . 4
A.1 Data Acquisition . . . 5
A.2 Mapping the Low- and High-Density Carbon Network . . . 6
B Two-Point Correlation Function . . . 7

3 Capacitance Assessment from Cyclic Voltammetry (CV) and Galvanostatic Charge-Discharge (GCD) Measurements **8**
A Equivalent R-C Circuit Model . . . 8
B Steady-State Solution for Cyclic Voltammetry (CV) . . . 9
C Fractional Model for Galvanostatic Charge-Discharge Cycles (GCD) . . . 11
D Coulombic Efficiency and Capacitance Retention from GCD Measurements . . . 12
E Discussion of Maximum Energy Storage . . . 13
F Discussion and Additional Experimental Results of Capacitance Measurements: nCB-Threshold Values. Effect of Aging on Capacitance Measurements . . . 14
G Discussion of Limitation of the Model-Based Approach . . . 14

4 Dimensional Analysis and Scaling **15**
A Dimensional Analysis of Rate-Independent Capacitance . . . 15
B Scaling of Rate Capability . . . 15

A APPENDIX **16**
A Fractional Derivatives . . . 16
B Some relevant Laplace Transforms . . . 16

1. Carbon-Cement Materials and Electrodes

A. Sample Preparation. Materials were prepared as a dry mix of Portland cement powder (C) and nano-carbon black (nCB), at defined nCB-to-C (nCB/C) mass ratios. Water was then combined with the superplasticizer (a polynaphthalene sulfonate (PNS)-based HRWRA (high-range water-reducing admixture)) under continuous stirring to obtain a target Water-to-Cement (W/C) mass ratio. The specific quantity of PNS included in the sample preparation was selected based on recommendations from previous studies for optimum conductivity (see (1)). The fresh cement-carbon paste was cast into a polycarbonate mold of 2.2 cm diameter, which defined the geometric area ($A = 3.8$ cm^2) of the electrodes. The samples were sealed with parafilm on both ends and immersed in a lime/water solution during the hydration process. Hardened samples were demolded after at least 28 days, following standard concrete engineering protocols. The electrodes were then cut with a slow-speed diamond saw to a specified thickness and the surface of the samples was polished with a sequence of SiC papers of decreasing abrasiveness. Such prepared samples were used for Energy Dispersive Spectroscopy (EDS), Raman spectroscopy, and micro-indentation measurements. For capacitance measurements, the samples, playing the role of electrodes, were additionally saturated in an electrolyte solution (1M KCl), and placed in a measurement device (Fig. 2.A in the main text). Selection of KCl as the electrolyte was due to its neutral pH, aiming to minimize potential impacts on the cement paste microstructure. By avoiding the use of acidic solutions and instead opting for KCl, the electrolyte was both effective for its intended application, while simultaneously ensuring compatibility with the cement paste. Additionally, KCl is characterized by a relatively high diffusion coefficient (see the main text), which is advantageous for our supercapacitor performance.

	BET (Ar)	NLDFT (Ar/CO_2)				
Sample	S_{BET} m^2/g	S_{NLDFT} m^2/g	Sub-nano m^2/g	Micro m^2/g	Meso m^2/g	Peak Å
PBX 55 (2)	52	54	18	27	27	8
Vulcan (3)	241	241	138	188	53	6–7
Ketjen (4)	1,307	1162	404	665	497	7

Table S1. Pore size, volume and surface area measurements of three different carbon blacks, which differ primarily in their specific surface areas (BET and Non-Local Density Functional Theory (NLDFT) methods were used for the determination of the specific surface areas). The results were obtained based on Argon adsorption at 87K (for the BET); and Argon adsorption at 87K and CO_2 adsorption at 273K using the dual-fit method developed by Jagiello et al. (5) (for the NLDFT method).

B. Carbon-Cement Electrodes and Constituent Properties. A total of 5 different carbon/cement material formulations were designed, mixed and cured to prepare 8 electrodes of different thicknesses. To identify the electrode samples, the following electrode naming convention was adopted:

$$\text{Type nCB/C } (W/C) - \text{Electrode Thickness, } d \qquad [1]$$

where the first three identifiers specify the material (type of carbon black, nCB/C mass ratio (in%), W/C mass ratio), whereas the last one defines the total thickness of two electrodes, d. Three different types of nano Carbon Black materials (nCB-Material) were investigated:

- PBX-55 carbon black produced by Cabot Corporation (2).
- Vulcan XC72 carbon black produced by Cabot Corporation (3).
- Ketjenblack EC-600JD carbon black produced by Nouryon Corporation (4).

The three types of carbon black differ in their specific surface areas, which were determined independently by B.E.T. and the Non-Local Density Functional Theory (NLDFT) method (5) of powder analysis (Tab. S1). More specifically, while all carbon black materials exhibit a pore size peak around $6 - 8 \times 10^{-10}$ m (Fig. S1), they differ primarily in their specific surface areas (Tab. S1).

Five different carbon/cement material formulations were designed, mixed and cured for the preparation of eight electrodes of different thickness. They can be re-grouped in three categories, listed in Table S2:

- Three electrode samples to study the effect of the W/C ratio, while maintaining the nCB/W mass ratio constant;
- Five electrode samples to study the effect of electrode thickness; three made with PBX 55, and two made with Ketjenblack;
- Three samples to study the effect of the carbon type: PBX 55, Vulcan XC72, Ketjenblack EC-600JD;

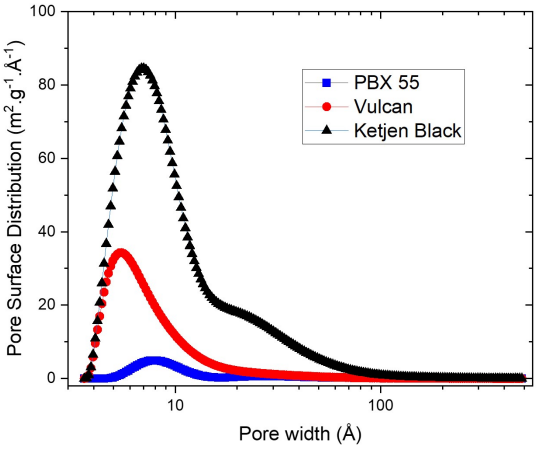

Fig. S1. Pore size distribution of three types of carbon black.

Sample Name	W/C	nCB/C	CB-Type	d/cm	C/(g.cm^{-3})	W/(g.cm^{-3})	nCB/(g.cm^{-3})
	Effect of W/C Ratio						
PBX 22.4 (0.8) - 0.26	0.8	0.224	PBX 55 (2)	0.26	0.80	0.64	0.18
PBX 16.8 (0.6) - 0.25	0.6	0.168	PBX 55 (2)	0.25	0.98	0.59	0.16
PBX 10.1 (0.42)- 0.25	0.42	0.101	PBX 55 (2)	0.25	1.25	0.52	0.13
	Effect of Electrode Thickness						
PBX 22.4 (0.8) - 0.18	0.8	0.224	PBX 55 (2)	0.18	0.80	0.64	0.18
PBX 22.4 (0.8) - 0.26	0.8	0.224	PBX 55 (2)	0.26	0.80	0.64	0.18
PBX 22.4 (0.8) - 1.00	0.8	0.224	PBX 55 (2)	1.00	0.80	0.64	0.18
KB 12.8 (1.4) - 0.34	1.4	0.128	Ketjen (4)	0.34	0.56	0.78	0.07
KB 12.8 (1.4) - 0.60	1.4	0.128	Ketjen (4)	0.60	0.56	0.78	0.07
	Effect of Type of Carbon Black						
PBX 22.4 (0.8) - 0.26	0.8	0.224	PBX 55 (2)	0.26	0.80	0.64	0.18
KB 12.8 (1.4) - 0.34	1.4	0.128	Ketjen (4)	0.34	0.56	0.78	0.07
Vulcan 16 (0.8) - 0.4	0.8	0.160	Vulcan (3)	0.40	0.82	0.66	0.13

Table S2. List of electrode samples and mix design: W/C = Water-to-Cement mass ratio, nCB/C = nanocarbon black -to- cement mass ratio. d is the thickness of two electrodes. The 'effective' mass density of cement (C), water (W) and carbon black (nCB) was determined considering the mass density values of cement, $\rho_{\mathbf{CEM}} = 3.15$ g.cm^{-3}, and carbon black, $\rho_{\mathbf{C}} = 1.7$ g.cm^{-3}.

C. Microindentation. For mechanical analysis, instrumented microindentation was employed (Anton Paar Instruments). All tests were carried out with a Berkovich diamond tip. Microindentation tests were performed on samples PBX 10.1 (0.42), PBX 16.8 (0.6), and PBX 22.4 (0.8). Tests were operated to a maximum indentation force of $P = 20$ N on polished samples, following standard procedures of surface preparation for indentation analysis (6). The hardness, $H = P/A$, was determined from the maximum load divided by the contact area estimated by the Oliver-Pharr method (7). A total of 10 tests per sample were performed, providing mean values of $H = 0.43, 0.21$ and 0.11 GPa for samples prepared with increasing W/C-ratio of 0.42, 0.6 and 0.8, and the standard deviation was smaller than 10% of the mean value. These values are displayed in Fig. 2.F in the main text, and fit to a dimensionless power function:

$$\frac{H}{H_0} = \left(\frac{1 + \overline{\rho}_{\text{cem}} W/C}{1 + \overline{\rho}_{\text{cem}} (W/C)_0} \right)^{\gamma} \quad [2]$$

where $\overline{\rho}_{\text{cem}} = 3.15$ is the specific mass density of cement; and H_0 is the hardness of the material prepared at $W/C = 0.42$. The exponent obtained by the fit is $\gamma = 3.28$, consistent with values of strength scaling reported in the cement literature (see e.g. (8)).

2. Texture Analysis

In this section, we provide details regarding the texture analysis of the nCB particle network by applying the two-point correlation function, $S_2(r)$, to images of the nCB network generated by our correlative EDS-Raman spectroscopy approach. The technique is first presented, and the application of the two-point correlation function is shown thereafter.

A. Correlative High Vacuum EDS–Raman Spectroscopy. The nCB network was visualized by combining Energy Dispersive Spectroscopy (EDS) with Confocal Raman Microscopy (CRM) techniques. The coupling of these two different techniques aims at leveraging the advantage of each method. Namely:

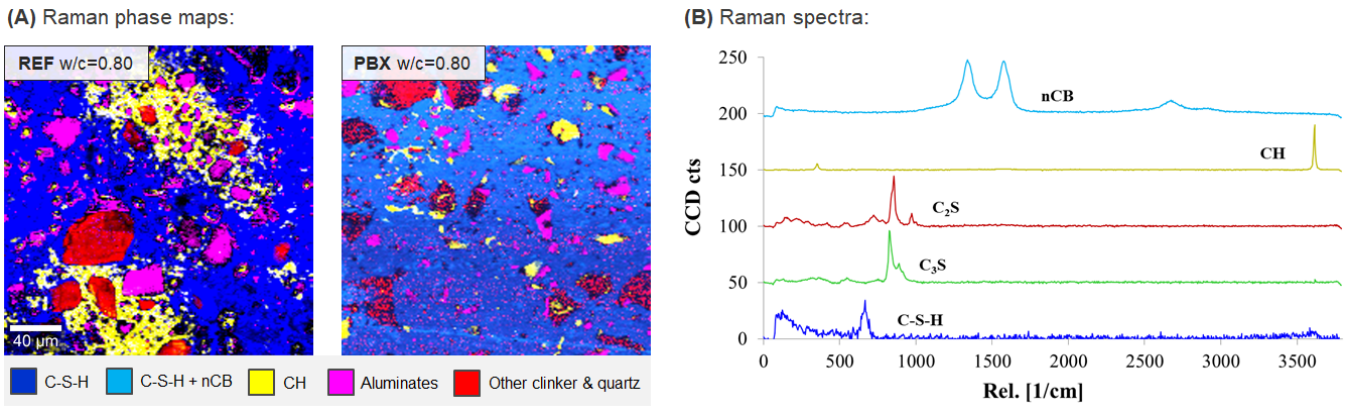

Fig. S2. Raman spectroscopy: (A.) phase maps of the reference (W/C=0.80) and carbon-cement samples, (B.) Raman spectra of main phases: C-S-H, clinker (C_3S, C_2S), portlandite (CH) and nano-carbon black (nCB).

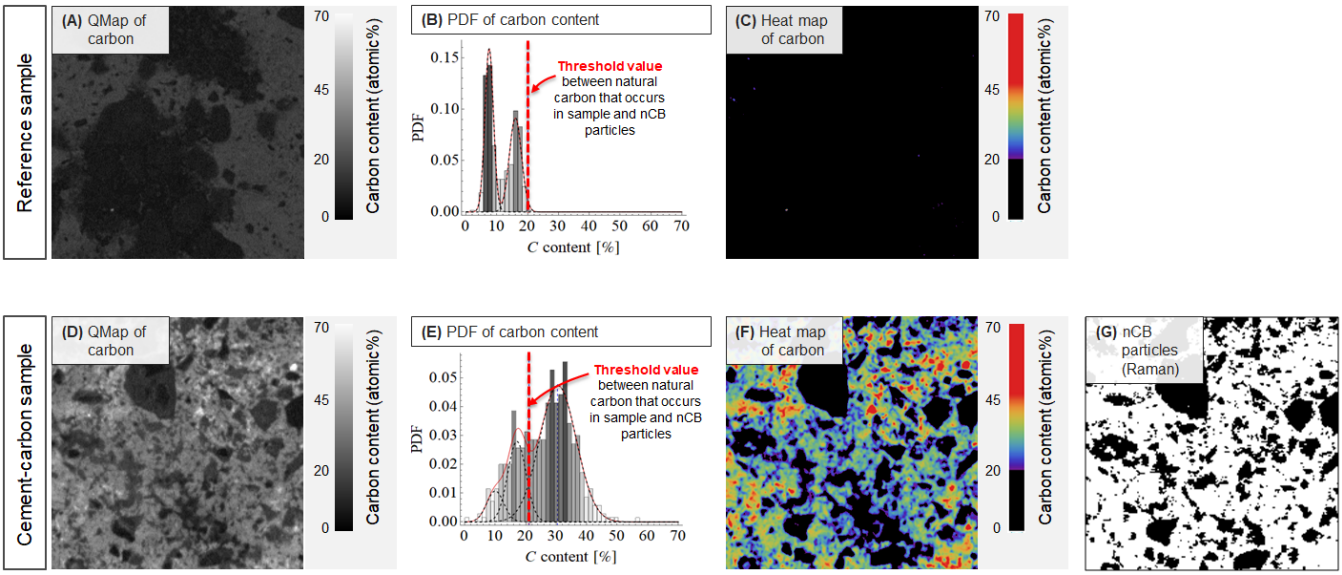

Fig. S3. Carbon content comparison between a reference sample (without nCB particles) and an electrode (carbon-cement system): (A.),(D.) quantification map (QMap) of carbon (based on EDS data), (B.),(E.) probability density function (PDF) of carbon intensity, (C.),(F.) heat map of carbon, and (G.) segmented nCB particles based on Raman spectroscopy. Carbon content is presented in atomic %.

- EDS is a scanning electron microscopy-based technique that is routinely used to analyze and map the elemental distribution of a specimen's surface. Due to its high resolution, it is extremely useful in the elemental mapping of cementitious materials (9). However, due to the intrinsic complexity of the microstructure of cementitious materials, the identification of the different phases is still a challenge. Therefore, coupling EDS with other techniques, e.g. Raman spectroscopy, can be very useful for phase identification, especially in the case of a complex mixtures, such as the cement system with nCB particles investigated herein.

- Raman spectroscopy is a vibrational spectroscopy technique that is commonly used in the characterization of a variety of materials, including cementitious composites (10) and nCB particles (11). The technique is based on the interaction of monochromatic laser light with the electron clouds of the molecules in the sample which can provide detailed information about the vibrational modes of the investigated material. Raman spectroscopy has proven to be an excellent tool for mapping the spatial distribution of amorphous and crystalline phases of cementitious composite with a submicron resolution (10). This technique can also provide a wealth of information that is crucial for understanding the structure and properties of nCB particles. For example, it can be used to determine the degree of order and disorder in the carbon structure based on the Raman spectra features, e.g., on the characteristics of the pair of bands at ~ 1360 cm^{-1} and ~ 1580 cm^{-1} referred to in the literature as the D and G bands, respectively (12). The presence of the D band is assigned to structural defects, and it has been shown that the intensity of the D band relative to that of the G band increases with the amount of disorder. As a result, the intensity ratio, I_D/I_G, has often been used to characterize the average crystal planar domain size L_a (13, 14).

A.1. Data Acquisition. Sample surfaces were polished prior to testing using a sequence of polishing pads with reduced abrasiveness. Silicon carbide grinding papers were first employed with a grit of P2500 and P4000, followed by aluminum oxide discs with a particle size of 3 μm and 1 μm.

In this work, we first acquired EDS mapping data from the different electrode materials using a Vega3 XMU (Tescan, Czech Republic) scanning electron microscope. For this purpose, the high vacuum mode and 15 keV accelerating voltage were employed. EDS elemental composition maps (240×240 μm, resolution of 0.468 μm/px) were acquired with a Bruker XFlash 630 silicon drift detector with an acquisition time of 7 hours to ensure a minimum of 3,000 counts per pixel. Collected EDS data were quantified with the Bruker Esprit 2.1 software with PB Linemarker-ZAF correction. As a result, quantification maps (QMaps), expressed in atomic %, of carbon and other relevant elements (Ca, Si, Al, Fe, Mg, K, Te, and Na) were obtained.

Second, Raman spectra were collected with a CRM system (Alpha 300RA; WITec, Germany) utilizing a Nd:YAG laser ($\lambda =$ 532 nm) and a 50× Zeiss objective. The excitation wavelength was calibrated using a silicon wafer standard. Raman maps of the same electrode samples used for the EDS analysis were collected over a 200×200 μm size region (resolution of 1 μm/px). The maps were acquired with a continuous laser beam and an accumulation time of 0.23 s per point. WITec Project 5 and Matlab software were used for data analysis and visualization. The software's built-in k-means clustering function was used to identify the component spectra of each scan (see Fig. S2).

Third, EDS maps were overlapped with Raman maps in order to improve phase identification. For this purpose, Matlab software was utilized. To match the Raman phase maps of the nCB phase with the EDS maps of carbon content (with the

precision of $< 1\mu$m), a shift in x and y directions as well as rotation angle were established based on semi-automatic procedure using characteristic features of the images, e.g., unhydrated clinker inclusions.

This three-step procedure was applied to the five electrode materials investigated in this study (PBX 10.1 (0.42), PBX 16.8 (0.60), PBX 22.4 (0.80), Vulcan 16.0 (0.80), and KB 12.8 (1.40), see Tab. S2), as well as to a pure cement-based reference sample prepared at W/C=0.80 (without nCB).

Furthermore, Raman spectra were also acquired from pure nCB powders (PBX-55, Vulcan XC72, and Ketjenblack EC-600JD, see Tab. S1) placed on glass microscope slides. Specifically, after background removal, Gaussian distribution functions were fitted to the spectra (Fig. S4) to evaluate the D -to- G band intensity ratio, I_D/I_G, based on the integrated areas. This approach allowed us to characterize the average crystal planar domain size L_a (size of the graphitic coherent domains perpendicular to the c-axis) using the relation formulated by Knight and White (15) and based on the work of Tuinstra and Koenig (11) (with the coefficient 4.4 for the green laser):

$$L_a = \frac{4.4}{I_D/I_G} \quad [3]$$

L_a for the three carbon black powders employed in this study are as follows: 4.38 nm (PBX-55), 2.60 nm (Vulcan XC72), and 2.73 nm (Ketjenblack EC-600JD). It is worth noting that the used formula is a first approximation of the L_a (16, 17) and can only be used for well ordered carbon materials with L_a >2 nm. The obtained Raman spectra and their characteristics for nCB used in this study are very similar to those obtained from activated charcoal reported in (11) or (15). Also, the 60-70% higher I_D/I_G ratios for Vulcan and Ketjenblack nCB demonstrate their more disordered structure when compared to PBX nCB. Finally, the fact that the I_D/I_G ratio of the pure nCB powder (Fig. S4) match the one of nCB incorporated in the cementitious matrix (Fig. S2B and Fig. 1A in the main manuscript) provides evidence of the non-reactivity of carbon black in the alkaline environment of cement-based materials.

A.2. Mapping the Low- and High-Density Carbon Network. The correlative EDS–Raman approach provides us with a phase map of ~0.5 μm/px resolution. At this scale, nCB (characterized by a size of < 100 nm) is intermixed with C-S-H and other hydration products. The intermixed particles of nCB can be identified in regions with a high concentration of carbon on the EDS maps. However, in order to obtain information regarding the nCB network structure, the background carbon content must first be subtracted. This background carbon content is obtained from a carbon map of the reference sample without nCB particles (Fig. S3A). This background carbon signal likely originates from the carbonation of hydration products following reaction with atmospheric CO2 during sample preparation. From the probability density function (PDF) of carbon content for the reference sample shown in Fig. S3B it is found that the background carbon consists of two clusters, one below 10% and one in the range $10 - 20\%$. These two families could be caused by, among other factors, different carbonation kinetics of various cement phases. Compared to this background carbon, the electrode samples additionally contain a clear third family of carbon content exceeding 20% and reaching up to 60%, see Figs. S3.D-E. This family represents the nCB phase (nCB particles intermixed with hydration products at the observed resolution). To characterize this nCB phase, we processed the data using a two-step procedure: First, a Gaussian mixture fit of the carbon concentration was performed using the cumulative distribution function (CDF)-based approach in which the difference between the experimental CDF and the model CDF was minimized to identify the different phases (see e.g. (18)). Second, the identified clusters were mapped and confirmed from Raman maps obtained from the nCB particles (Fig. S3G) based on their characteristic Raman spectra (peaks in the range of 1200-1700 cm^{-1}), shown in Fig. S2B. Specifically, we confirmed that this nCB phase exhibited the same I_D/I_G-ratio as the pure nCB powder (Fig. 1.A in main text).

After removal of the background carbon (note that the subtraction process was applied uniformly to all phases, without differentiation based on their calcium content or carbonation susceptibility) in the high-vacuum EDS carbon maps, the heat map of the in-situ nCB phase in the electrode sample showed that the carbon concentration was not uniform, but rather exhibited a high variability with spots of high carbon concentration connected by strings of carbon of lower concentration (Fig. S3F). This variability in carbon content is most likely not related to a variability in physical density of the nCB particles,

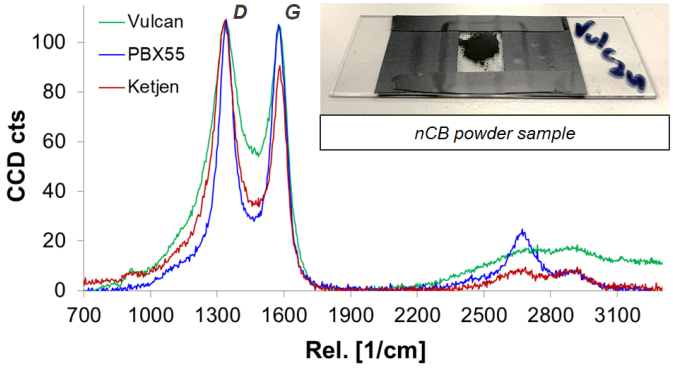

Fig. S4. Raman spectra of investigated nCB powders: PBX-55, Vulcan XC72, and Ketjenblack EC-600JD.

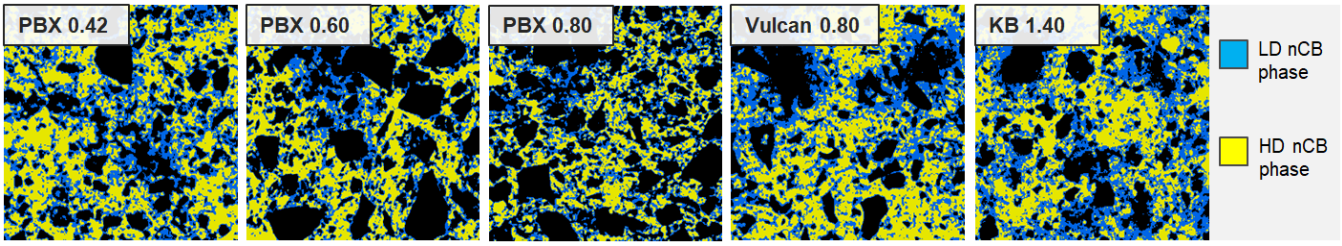

Fig. S5. Segmented maps of low- and high-density nCB phases for all investigated samples: PBX 10.1 (0.42), PBX 16.8 (0.60), PBX 22.4 (0.80), Vulcan 16.0 (0.80), and KB 12.8 (1.40).

but rather to the organization of nCB particles in the form of a connected carbon network. To capture this variability in our texture analysis, we separate the nCB phase into a low-density (LD) and a high-density (HD) carbon phase, using as threshold the mean value of the carbon concentration obtained by a Gaussian mixture fit (see Fig. 1.C in main text). The segmented LD- and HD- nCB phases for all investigated samples are displayed in Fig. S5.

B. Two-Point Correlation Function. For texture analysis of the nCB network, we assumed statistical isotropy, and used the two-point correlation function to spatially correlate two points of the nCB network by their distance $r = |r_i - r_j|$ (19):

$$S_2(r = |r_i - r_j|) = \langle I(r_i)\, I(r_j) \rangle \quad [4]$$

where $I(r_i)$ is the indicator function: $I(r_i) = 1$ if $r_i \in C$, and $I(r_i) = 0$ otherwise, with C being the domain under consideration (here, the previously identified low-density or high-density nCB phase, as shown in Fig. S5). The two-point correlation function provides access to a number of important texture parameters, including the phase concentration (20, 21):

$$\phi_i = S_2(r = 0) \quad [5]$$

the mean chord length:

$$\ell_i = \langle zp(z) \rangle = -\frac{\phi_i}{S_2'(0)}; \qquad S_2'(0) = \frac{\mathrm{d}S_2}{\mathrm{d}r}|_{r=0} \quad [6]$$

and the (texture) specific surface (of dimension L^{-1}):

$$s_i = -\pi S_2'(0) \quad [7]$$

where subscript $i = LD, HD$ refers to the LD or HD carbon phase, $p(z)$ is the chord length probability distribution, and $S_2'(0)$ is the slope of $S_2(r)$ at the origin.

The $S_2(r)$ function was implemented for binary images (512 × 512 px) of the LD- and HD-nCB phase obtained from correlated high-vacuum EDS-Raman maps on the 240×240 μm regions (Fig. S5). The image size and resolution emerge from EDS QMaps of carbon, and the calculation of $S_2(r)$ uses the algorithm proposed by Yeong and Torquato (22). This algorithm samples along two orthogonal directions (the rows and columns of the pixelated image) while respecting periodic boundary conditions. Given isotropy, such an approach was found to be more accurate and results in a smoother $S_2(r)$ profile compared to random sampling (using Monte-Carlo simulations). For statistically isotropic systems, it provides similar results as recent developments using fast Fourier transforms (23–25).

Material Sample	ϕ_{LD}	ϕ_{HD}	ℓ_{LD} [μm]	ℓ_{HD} [μm]
PBX 22.4 (0.80)	0.250	0.241	1.922	3.532
PBX 16.8 (0.60)	0.240	0.302	2.124	4.383
PBX 10.1 (0.42)	0.329	0.368	2.615	4.931
PBX 10.1 (0.42)[a]	0.326	0.373	2.591	4.998
PBX 10.1 (0.42)[b]	0.309	0.329	2.499	4.538
KB 12.8 (1.40)	0.381	0.342	3.135	4.583
Vulcan 16.0 (0.80)	0.336	0.342	3.031	5.012

[a],[b] - additional repetitions at different regions

Table S3. Texture properties of carbon network obtained from two-point correlation function, $S_2(r)$.

Detailed values of ϕ_i and ℓ_i for all investigated samples are reported in Table S3, with the following caveats: (1) The phase concentrations are representative of the carbon network at the scale of the experimental resolution, and should not be interpreted as representing the actual volume fraction of carbon black in the samples. (2) While LD- and HD- nCB phases were obtained by separating a Gaussian of carbon content at its mean value, their concentrations ϕ_i are not equal. This is due to both the noise in background carbon (see Fig. S3E), and the deviation of the actual distribution from the assumed Gaussian

distribution. (3) The mean chord length ℓ_i is 4 to 10 times greater than the adopted resolution of the binary images, and as such, the chord length and any other parameter we derive from it (such as the texture specific surface) is representative of the texture of the carbon network at the $\sim$0.5 μm resolution level. (4) Experimental repeatability was assessed by determining $S_2(r)$ and the corresponding texture parameters, ϕ_i and ℓ_i for three different areas of the same sample (PBX 10.1 (0.42); see Tab. S3). The low coefficient of variations of 2.7%, 5.5%, 1.9%, and 4.2% for ϕ_{LD}, ϕ_{HD}, ℓ_{LD}, and ℓ_{HD}, respectively, confirm the repeatability and statistical isotropy of the nCB-network's texture.

3. Capacitance Assessment from Cyclic Voltammetry (CV) and Galvanostatic Charge-Discharge (GCD) Measurements

In this section we show the derivation of the analytical solutions we use in order to extract capacitance values from cyclic voltammetry (CV) and galvanostatic charge-discharge measurements.

A. Equivalent R-C Circuit Model. Most quantitative capacitance models are based on an equivalent R-C circuit in which a resistor, R, is in series with a capacitor, C (see e.g. (26–29)). The resistor represents the sum of all resistances present (interstitial solution and solids), whereas the capacitor is representative of an electric double layer capacitor (EDLC), composed of two electrodes saturated by an electrolyte, and separated by an insulator. The two electrodes are connected to an outside potential difference, denoted by U, charging one electrode with a positive charge, the other with a negative charge. The associated current is denoted by I. We frame the problem in the context of Boltzmann's integrodifferential equations, and we link current I to the potential difference U by means of the convolution integral:

$$U(t) = \int_{-\infty}^{t} \mathcal{R}(t-t') \frac{\mathrm{d}I}{\mathrm{d}t'} \, \mathrm{d}t' \qquad [8]$$

where the kernel, $\mathcal{R}(t-t')$, is the time-dependent resistance function, accessible in a GCD test carried out at constant current $I(t) = I_0$. In fact, the Laplace transform of Eq. (8) provides Ohm's law in Laplace domain, $\widehat{U}(s) = s\widehat{\mathcal{R}}(s)\,\widehat{I}(s)$, where $s\widehat{\mathcal{R}}$ is the s-multiplied resistance function in Laplace domain. The solution procedure in Laplace domain is known as 'correspondence principle', and has a wide-spread use in e.g. linear viscoelasticity problems (30): an Ohm's solution remains valid in Laplace domain provided one replaces resistance by the s-multiplied resistance function. This resistance function is obtained from the R-C circuit equations:

$$I(t) = C\frac{\mathrm{d}U_C}{\mathrm{d}t}; \qquad I(t) = \frac{1}{R}(U(t) - U_C(t)) \qquad [9]$$

where $U_C(t)$ is the part of the total potential difference U stored into the electrodes, resistance R defines the instantaneous response, whereas capacitance C characterizes the time-dependent charge storage response. The characteristic time of the capacitor is $\tau = CR$. A Laplace transform of Eq. 9 provides:

$$\widehat{I}(s) = sC\widehat{U}_C(s); \qquad \widehat{I}(s) = \frac{1}{R}(\widehat{U}(s) - \widehat{U}_C(s)) = \frac{1}{s\widehat{\mathcal{R}}(s)}\widehat{U}(s); \qquad s\widehat{\mathcal{R}}(s) = R\frac{1+s\tau}{s\tau}; \qquad \mathcal{R}(t) = R\left(1 + \frac{t}{\tau}\right) \qquad [10]$$

The simple example of the linear equivalent R-C circuit illustrates the ease of use of the framework. It will turn out most useful, when considering fractional derivatives. In fact, consider for $\mathcal{R}(t)$ the following expression (31):

$$\mathcal{R}(t) = R\left(1 + \frac{1}{\Gamma_{1-\alpha}}\left(\frac{t}{\tau}\right)^{-\alpha}\right) \qquad [11]$$

where R and τ are constants, and $\Gamma_x = \Gamma(x)$ is the complete Gamma function. Use of Eq. (11) in Eq. (8) provides the fractional integral (31):

$$U(t) = U^+ + \frac{R\tau^\alpha}{\Gamma_{1-\alpha}} \int_{-\infty}^{t} (t-t')^{-\alpha} \frac{\mathrm{d}I}{\mathrm{d}t'} \, \mathrm{d}t' \qquad [12]$$

where U^+ stands for the voltage after instantaneous charge or discharge, while the second term stands for the non-instantaneous part of the potential difference stored into the electrodes, defined by the fractional exponent, $\alpha \in]0,1]$. Hence, expression (12) stays true to the serial arrangement of a resistor, providing an instantaneous response, U^+, and a capacitor the evolution of which is governed by a fractional derivative:

$$I(t) = \frac{\tau^\alpha}{R}\frac{\mathrm{d}^\alpha U_C}{\mathrm{d}t^\alpha}; \qquad I(t) = \frac{1}{R}(U(t) - U_C(t)) \qquad [13]$$

B. Steady-State Solution for Cyclic Voltammetry (CV). We are interested in the steady state solution when a constant scan rate, $u = U_0/t_0$, is applied over a charge time t_0, from $U = 0$ to $U = U_0$, and then reversed. To derive an analytical solution, we employ the linear rate equation (9). Specifically, the linearity of applied voltage with time suggests a change in variable replacing time derivatives in the rate equation (9) by derivatives w.r.t. the voltage U:

$$I(t) = C\frac{\mathrm{d}U_C}{\mathrm{d}t} = C\frac{\partial U_C}{\partial U}\frac{\mathrm{d}U}{\mathrm{d}t} = \lambda|u|C\frac{\mathrm{d}U_C}{\mathrm{d}U} \quad [14]$$

where the applied voltage rate, $\mathrm{d}U/\mathrm{d}t$, is a constant; i.e. $\mathrm{d}U/\mathrm{d}t = \lambda|u|$ with $\lambda = \mathrm{sign}(\mathrm{d}U/\mathrm{d}t)$. By combining Eqn. (9) and (14), we obtain the governing differential equation:

$$\overline{I} = \overline{U} - \overline{U}_C = \frac{\lambda}{\bar{t}_0}\frac{\mathrm{d}\overline{U}_C}{\mathrm{d}\overline{U}} \quad [15]$$

where $\overline{I} = I/(U_0/R)$, $\overline{U} = U/U_0 \in]0,1[$, $\overline{U}_C = U_C/U_0$ and $\bar{t}_0 = t_0/\tau$ are dimensionless expressions of the current, the applied potential difference, the capacitance voltage, and the charge–discharge ramp duration, respectively. The solution of this differential equation is:

$$\overline{U}_C = \overline{U} - \frac{\lambda}{\bar{t}_0}(1 - k_1\exp(-\lambda\bar{t}_0\Delta\overline{U}) \quad [16]$$

$$\overline{I} = \overline{U} - \overline{U}_C = \frac{\lambda}{\bar{t}_0}(1 - k_1\exp(-\lambda\bar{t}_0\Delta\overline{U}) \quad [17]$$

where $\Delta\overline{U}$ is the change in applied voltage with reference to the initial voltage of the charge ($\overline{U}(0, \lambda = 1) = 0$) and discharge ($\overline{U}(0, \lambda = -1) = 1$):

$$\Delta\overline{U} = \overline{U} - \overline{U}(0) = \overline{U} - \frac{1}{2}(1 - \lambda) \quad [18]$$

The integration constant, $k_1 = k_1(n, \lambda)$ depends on the charge-discharge cycle, n, and on the sign, $\lambda = \mathrm{sign}(\mathrm{d}U/\mathrm{d}t)$, and remains to be determined from the continuity of the current at the moment of charge-discharge, as well known from earlier developments [see Eq. (1) in Ref. (27)], that have been used for a variety of purposes, incl. the determination of the 'effective' surface area for double layer charge storage onto oxide layers (27), the assessment of the ionic resistance in a porous electrode (26), and so on. The added value of our general solution will come to light in the subsequent development of the expression of k_1 for steady-state conditions.

Consider the first cycle. The initial conditions of the charge phase ($\lambda = 1$) are $\overline{U}(0) = \overline{U}_C(0) = \overline{I} = 0$. Hence, $k_1(n = 1, \lambda = 1) = 1$, and therefore (see Eq. [17]):

$$\overline{I}(\overline{U}) = \frac{1}{\bar{t}_0}\left(1 - \exp(-\bar{t}_0\overline{U})\right) \quad [19]$$

Current continuity at the moment of discharge entails:

$$k_1(n = 1, \lambda = -1) = 2 - k_1(n = 1, \lambda = 1)\exp(-\bar{t}_0)) \quad [20]$$

In a similar fashion, continuity of the current between charge-discharge phase of the n^{th} cycle, [i.e., $\overline{I}(n-1, -1, \Delta\overline{U} = -1) = \overline{I}(n, 1, \Delta\overline{U} = 0)$ and $\overline{I}(n, 1, \Delta\overline{U} = 1) = \overline{I}(n, -1, \Delta\overline{U} = 0)$], entails:

$$k_1(n, \lambda = 1) = 2 - k_1(n-1, \lambda = -1)\exp(-\bar{t}_0) \quad [21]$$

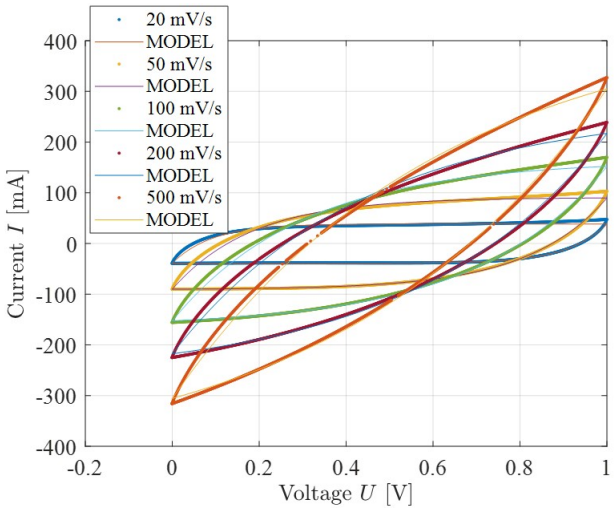

Fig. S6. Current-Voltage (CV) measurements and model fits for different sweep rates $u = U_0/t_0$ [Electrode: KB 12.8 (1.4) - 0.34, see Tab. S2].

$$k_1(n, \lambda = -1) = 2 - k_1(n, \lambda = 1)\exp(-\bar{t}_0) \quad [22]$$

Under steady-state conditions, the integration constants do no more evolve with cyclic loading; that is, $k_1(n, \lambda = 1) = k_1(n-1, \lambda = 1)$ and $k_1(n, \lambda = -1) = k_1(n-1, \lambda = -1)$. The steady-state condition thus provides a simple closed-form solution for the integration constant for charge-discharge:

$$k_1(n, \lambda = \pm 1) = \frac{2(1 - \exp(-\bar{t}_0))}{1 - \exp(-2\bar{t}_0)} \quad [23]$$

with $k_1(\bar{t}_0 \to \infty) = 2$ and $k_1(\bar{t}_0 \to 0) = 1$. That is, Eqn. (16), (17) and (23) provide a convenient way to fit cyclic current–voltage (CV) curves carried out at different constant voltage sweep rates $u = U_0/t_0 = U_0/(\tau \bar{t}_0)$. This is illustrated in Figure S6.

While the CV-fits work rather well (on-average over the entire voltage sweep), it is common practice to estimate the capacitance from the integral of the CV-curve, in form of the so-called integral capacitance [see, for instance, (32)]:

$$C_{\text{int}} = \frac{\oint I \, \mathrm{d}U}{2u\, U_0} = \frac{\int_0^{U_0} I \, \mathrm{d}U}{u\, U_0} \quad [24]$$

where the second expression assumes perfect line symmetry between charge and discharge curve, associated with the absence of Faradeic effects; while the third expression We develop expression (24) in the form that permits an evaluation of the link between the integral capacitance, C_{int}, and the RC-circuit capacitance, $C = \tau/R$:

$$C_{\text{int}} = C\,\bar{t}_0 \int_0^1 \overline{I}\, \mathrm{d}\overline{U} = C\,\mathcal{F}(\bar{t}_0); \qquad \mathcal{F}(\bar{t}_0 = t_0/\tau) = 1 - \frac{1}{\bar{t}_0}\frac{2(1 - \exp(-\bar{t}_0))^2}{1 - \exp(-2\bar{t}_0)} \quad [25]$$

with $\mathcal{F}(\bar{t}_0 \to 0) = 0$; $\mathcal{F}(\bar{t}_0 \to \infty) = 1$, and a Taylor development around $1/\bar{t}_0 = \tau/t_0 \to 0$ in the form $\mathcal{F}(\tau/t_0) = 1 - 2\tau/t_0 + O((\tau/t_0)^2)$. Therefore, the integral capacitance is found to underestimate the capacitance of the RC-circuit.

In summary, we possess two means of determining, from CV-curves, the capacitance from fitting the CV curve and its area to the steady state solution:

$$\overline{I} = \frac{\lambda}{\bar{t}_0}\left(1 - \frac{2(1 - \exp(-\bar{t}_0))}{1 - \exp(-2\bar{t}_0)}\exp(-\lambda \bar{t}_0 \Delta\overline{U})\right) \quad [26]$$

$$\frac{C_{\text{int}}}{C} = R\bar{t}_0\frac{\oint I \mathrm{d}U}{2U_0^2} = 1 - \frac{1}{\bar{t}_0}\frac{2(1 - \exp(-\bar{t}_0))^2}{1 - \exp(-2\bar{t}_0)} \quad [27]$$

From an algorithmic point of view, we use Eqn. (26) and (27) in a nonlinear least-squares solver:

$$\min_{\bar{t}_0, 1/R}\left[\beta\frac{1}{N}\sum_N\left(I_i^{\text{exp}} - \frac{U_0}{R}\,\overline{I}(\bar{t}_0, \Delta\overline{U}_i)\right)^2 + (1-\beta)\left(\frac{[\oint I \mathrm{d}U]^{\text{exp}}}{2U_0} - \frac{U_0}{R}\frac{\mathcal{F}(\bar{t}_0)}{\bar{t}_0}\right)^2\right] \quad [28]$$

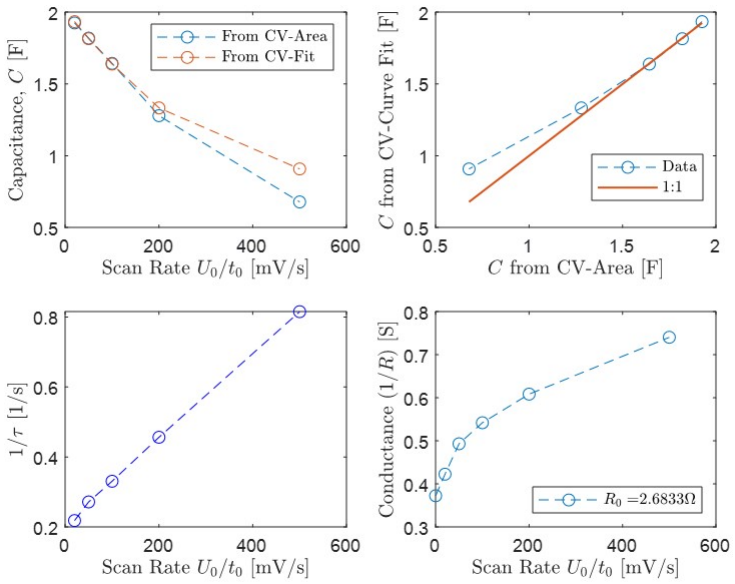

Fig. S7. Determination of scan rate dependent Capacitance from CV-Curve fits and CV-area, showing a linear scaling of $1/\tau$ vs. scan rate, and scan rate dependent conductance, $1/R$.[Electrode: KB 12.8 (1.4) - 0.34, see Tab. S2].

	Scan Rate $u = U_0/t_0$ in [mV/s]										Rate-Independent	
Sample Name	20		50		100		200		500		C_0/F	τ_0/s
PBX 22.4(0.8)-0.26	0.1627	0.1614	0.1625	0.1617	0.1608	0.1603	0.1584	0.1573	0.1491	0.1469	0.1634	1.450
PBX 16.8(0.6)-0.25	0.1334	0.1325	0.1318	0.1308	0.1291	0.1276	0.1222	0.1204	0.0979	0.0964	0.1344	2.817
PBX 10.1(0.42)-0.25	0.1079	0.1075	0.1019	0.1005	0.0909	0.0894	0.0721	0.0708	0.0489	0.0482	0.1119	9.743
PBX 22.4(0.8)-0.18	0.1230	0.1199	0.1219	0.1208	0.1217	0.1207	0.1223	0.1205	0.1164	0.1157	0.1214	1.092
PBX 22.4(0.8)-1.00	0.5735	0.5689	0.4364	0.4404	0.3069	0.3252	0.2000	0.2353	0.0920	0.1511	0.6554	21.490
KB 12.8(1.4)-0.34	1.9252	1.9343	1.8197	1.8153	1.6434	1.6386	1.2793	1.3334	0.6785	0.9085	1.9965	5.357
KB 12.8(1.4)-0.60	3.2911	3.3047	2.8033	2.8534	1.9199	2.2737	0.9924	1.6882	0.2885	1.1058	3.5746	14.480
Vulcan 16(0.8)-0.40	0.9361	0.9351	0.8100	0.8093	0.6599	0.6735	0.4667	0.5262	0.2017	0.3611	1.0154	10.582

Table S4. Rate-Dependent Capacitance values, $C(u)$ in units of [F], obtained from CV measurements for different scan rates from respectively CV area (first value) and CV-curve fit (second value) for tested carbon-cement electrodes. The last two columns present the rate-independent capacitance C_0, and the characteristic time $\tau_0 = C_0 R$ corresponding to the maximum energy storage.

where the first term (weighted by $\beta \in]0,1]$) minimizes the difference between the N experimental measurements and the model of the CV-curve (with $\Delta\overline{U}_i = U_i^{\rm exp}/U_0 - 1/2(1-\lambda)$), whereas the second term (weighted by $1-\beta$) minimizes the integral error. For each scan rate, $u = U_0/t_0$, this quadratic minimization provides a value for the conductance, $1/R$, and of the dimensionless time, $\bar{t}_0 = t_0/\tau$, from which we obtain the characteristic time, $\tau = t_0/\bar{t}_0$, and derive the capacitance $C = \tau/R$. To illustrate the algorithm, we display in Fig. S7(a-b), the capacitance obtained from the 'CV-curve fit' (first term in Eq. [28]); and compare the values with the capacitance values one obtains from the CV-areas (second term in Eq. [28]) using as input the experimentally available integral capacitance, $C_{\rm int}$, and the dimensionless time, $\bar{t}_0 = t_0/\tau$, obtained from quadratic minimization of the CV-curve fit ($\beta = 1$). The convergence of these two determination methods is shown in Fig. S7(a-b), with a perfect match between C obtained from respectively the 'CV-Curve Fit' and the 'CV-Area' for scan rates smaller than 200 mV/s. Fig. S7(c-d) display respectively the inverse of the characteristic time, $1/\tau$ and conductance $1/R$, used as minimization variables. Their dependence on the scan rate is a hallmark of the rate dependence of the capacitance accessible by CV-test.

Table S4 summarizes the capacitance measurement results obtained for all tested electrodes listed in Tab. S2.

C. Fractional Model for Galvanostatic Charge-Discharge Cycles (GCD). In a GCD-test a constant current, $I(t) = I_0$, is applied and reversed, while the voltage is measured in time. The linear model Eq. (9) provides the solution:

$$I_0 = C\frac{{\rm d}U_C(t)}{dt} = C\frac{{\rm d}U(t)}{dt} \qquad [29]$$

with $\bar{t} = t/\tau$. After instantaneous current loading, the voltage scales linearly with time:

$$\frac{U(\bar{t}>0)}{RI_0} = 1 + \bar{t} \qquad [30]$$

Similarly, after instantaneous current removal at time $\bar{t}_0 = t_0/\tau$:

$$\frac{U(\bar{t}>\bar{t}_0)}{RI_0} = \bar{t}_0 - (\bar{t} - \bar{t}_0) \qquad [31]$$

We note the jump (drop) in voltage at time $\bar{t} = \bar{t}_0$ of $[[U]] = U(\bar{t}_0^+) - U(\bar{t}_0^-) = -RI_0$. For the linear model, capacitance in a GCD-test is obtained from (33):

$$C = \frac{I_0}{{\rm d}U/{\rm d}t} = \frac{I_0\, t_0}{U(\bar{t}_0^+)} \qquad [32]$$

The linear model, however, has severe shortcomings to capture the visible non-linear evolution in time of the voltage after charge and discharge. This motivates us to consider the fractional model, Eq. [13]. More specifically, starting with the charge cycle, we make use of the property of Caputo's fractional derivative for a constant (see Appendix A, Eq. [60]), and obtain from Eq. [13] in time and Laplace domain:

$$RI_0 = \frac{{\rm d}^\alpha U}{{\rm d}\bar{t}^\alpha}; \qquad \widehat{U}(\bar{s}) = \frac{RI_0}{\bar{s}^{\alpha+1}} + \frac{U(0)}{\bar{s}} \qquad [33]$$

with $\bar{s} = s\,\tau$, and where we considered the Laplace transform of the instantaneously applied current through the Heaviside function $\mathscr{L}[I_0\,H(\bar{t})] = I_0/\bar{s}$ (with $H(\bar{t})$ the Heaviside function). The inverse Laplace transform reads (see Appendix B):

$$U(\bar{t}) = \frac{RI_0}{\Gamma_{1+\alpha}}\bar{t}^{\,\alpha} + U(0)\,H(\bar{t}) \qquad [34]$$

where $\Gamma_x = \Gamma(x)$ is the complete Gamma function [$\Gamma(2) = 1$].

Consider then a cyclic current application. The initial conditions are:

$$U_C(\bar{t}=0) = 0; \qquad U(\bar{t}=0^+) = RI_0 \qquad [35]$$

After (instantaneous) current loading,

$$U(\bar{t}>0) = RI_0\left(1+\frac{1}{\Gamma_{1+\alpha}}\bar{t}^{\alpha}\right) \quad [36]$$

Then, since $I_0 = (U-U_C)/R$, we readily obtain the capacitance voltage:

$$U_C(\bar{t}>0) = \frac{RI_0}{\Gamma_{1+\alpha}}\bar{t}^{\alpha} \quad [37]$$

At time $t=t_0$, consider an instantaneous drop of the current to $I=0$, i.e. the current load history:

$$I(\bar{t}) = I_0(H(\bar{t}) - H(\bar{t}-\bar{t}_0)) \quad [38]$$

with $\bar{t}_0 = t_0/\tau$ the dimensionless charge time. The charge phase is defined by Eqn. (36) and (37), whereas the discharge phase is evaluated from Eq. (34):

$$U(\bar{t}>\bar{t}_0) = -\frac{RI_0^d}{\Gamma_{1+\alpha}}(\bar{t}-\bar{t}_0)^{\alpha} + U(\bar{t}=\bar{t}_0^+)H(\bar{t}-\bar{t}_0) \quad [39]$$

Herein, the initial condition after unloading reads:

$$U(\bar{t}=\bar{t}_0^+) = RI_0\left(1+\frac{1}{\Gamma_{1+\alpha}}\bar{t}_0^{\alpha}\right) - RI_0^d \quad [40]$$

where the first term is the voltage before unloading $U(\bar{t}=\bar{t}_0^-)$ while the second term represents the voltage drop due to instantaneous unloading, $I(\bar{t}_0^-) = I_0 \rightarrow I(\bar{t}_0^+) = 0$. The (measurable) voltage for $\bar{t}>\bar{t}_c$ thus evolves as:

$$U(\bar{t}>\bar{t}_0) = \frac{RI_0}{\Gamma_{1+\alpha}}\left(\bar{t}_0^{\alpha} - (\bar{t}-\bar{t}_0)^{\alpha}\right) \quad [41]$$

Finally, since $I=(U-U_C)/R=0$, we immediately obtain the potential difference in the capacitor after discharge:

$$U_C(\bar{t}>\bar{t}_0) = U(\bar{t}>\bar{t}_0) \quad [42]$$

At time $\bar{t}=2\bar{t}_0$ the voltage is zero, and the process starts again.

In summary, for a constant applied current, $I(t)=I_0$, integration of the fractional derivatives provides:

$$U(t) = U^+ + \lambda\frac{RI_0}{\Gamma_{1+\alpha}}\begin{cases}\bar{t}^{\alpha}; & \text{for } 0\leq t/t_0\leq 1\\ (\bar{t}-\bar{t}_0)^{\alpha}; & \text{for } 1\leq t/t_0\leq 2\end{cases} \quad [43]$$

with $U^+ = U(t=0^+) = RI_0$ for charge ($\lambda=+1$) and $U^+ = U(t_0^+) = RI_0\bar{t}_0^{\alpha}/\Gamma_{1+\alpha}$ for discharge ($\lambda=-1$); while $\bar{t}=t/\tau$ is dimensionless time. The relevance of the fractional model can be seen from the fit of GCD-curves in Fig. S8.A. The figure also displays the fractional exponent for all our tested electrodes in function of the applied current (Fig. S8.B). Of interest is the observation that the fractional exponent converges to $\alpha\rightarrow 1$ for vanishing applied current. If we remind ourselves that a 'fractional capacitor' bridges the gap between a resistor, $\alpha=0$, and a true capacitor, $\alpha=1$, it is readily understood that the non-linearity of the GCD-response is due to the resistance of electrode activated at high applied current. Otherwise said, GCD-tests carried out at low applied current permit an assessment of the non-instantaneous energy storage of electrodes. This is illustrated in Fig. S8.C, displaying the capacitance determined from GCD-measurements, in function of the dimensionless current:

$$\frac{C(I)}{C_0} = 1 - \rho\frac{I_0\,d}{U_0\,A}\left(\frac{W}{C}\right)^{-2} \quad [44]$$

where C_0 = rate-independent capacitance (see main text), d, A = electrode thickness and area, W/C = water-to-cement ratio; while $\rho = 6.76\,\Omega$m is a fitted resistivity.

D. Coulombic Efficiency and Capacitance Retention from GCD Measurements. A close inspection of the GCD-measurements highlights the asymmetry of the charge-discharge response at low values of applied currents, known as Coulombic efficiency and defined in the GCD test as the time ratio between charge and discharge to reach a voltage of 1V, $CE = t_0^d/t_0^c$. We found that the Coulombic efficiency of our electrodes increases with increasing current (Fig. S9.A), attaining a Coulombic efficiency $>95\%$ during cyclic loading (Fig. S9.B). Furthermore, we also tested the capacitance retention in cyclic loading, defined here as the ratio of the capacitance after the n^{th}-cycle -to- the maximum capacitance measured during GCD-cycles (Fig. S9.C). We found that the capacitance is stable at $>95\%$ for at least 10,000 cycles, beyond which the capacitance declines, most likely due to electrolyte leakage. In fact, after 100,000 cycles the samples were found dry. This is a stark reminder that supercapacitors need to be saturated at all times to ensure long-term stability of the energy storage properties of the electrodes.

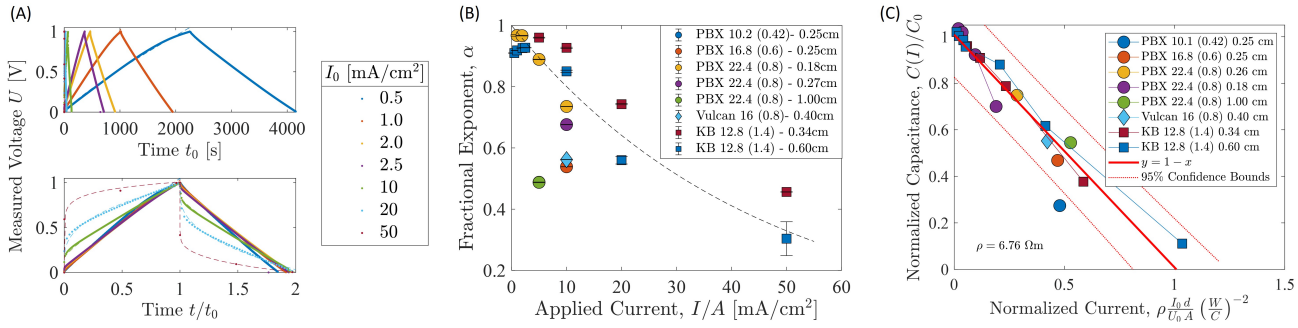

Fig. S8. Galvanostatic Charge/Discharge (GCD) Cycles: a constant current I_0 is applied and held constant until the current reaches $U = 1$ V. The current is then reversed until $U \to 0$.. (A.) Measurements (in time) and fractional model fits (in dimensionless time t/t_0) for electrode sample KB 12.8 (1.4) - 0.60. (B.) Fractional exponent α for all tested electrodes for 500 cycles (mean) with error bars representing one standard deviation. (C.) Normalized GCD-capacitance for all tested electrodes in function of (re-scaled) current. The data are fitted to a linear function.

E. Discussion of Maximum Energy Storage. The aim of this section is to prove Eq. [6] in the main text, which claims that the rate-independent capacitance provides the maximum amount of energy storage:

$$\max E = \frac{1}{2} C_0 U_0^2; \;\; C_0 = \lim_{u \to 0} C(u); \;\; U_0 = \lim_{I_0 \to 0} U(t_0^+) \qquad [45]$$

We start by recalling that it is common practice to define the energy storage of supercapacitors considering the total power:

$$P(t) = I(t)\, U(t); \qquad E_{\text{tot}} = \int_{t_1}^{t_2} P(t)\, \mathrm{d}t \qquad [46]$$

It should be noted, however, that this definition of energy storage includes both the instantaneous energy storage in the resistor, for instance $P(t_1^+) = R\, I(t_1)^2$, as well as the time-dependent storage of energy in the capacitor in form of a charged ion layer around the oppositely charged carbon black. Therefore, in order to derive the maximum energy storage capacity of our electrode materials, we consider only the time-dependent energy storage:

$$P_C(t) = I(t)\, U_C(t); \qquad E_C = \int_{t_1}^{t_2} P_C(t) \mathrm{d}t \qquad [47]$$

where I is the current and U_C the potential difference corresponding to the electrical charge stored into electrodes. To illustrate our purpose, consider the fractional EDLC model applied to a GCD-test. During charge with a constant current I_0, use of Eqn. [36] and [37] in [46] and [47] provides:

$$E_{\text{tot}}^{\text{GCD}}(t_0^-) = t_0 \frac{I_0^2}{R} + E_C^{\text{GCD}}(t_0^-); \qquad E_C^{\text{GCD}}(t_0^-) = \frac{\tau R\, I_0^2\, \bar{t}_0^{1+\alpha}}{(1+\alpha)\Gamma_{1+\alpha}} = C \frac{U(t_0^+)^2}{1+\alpha} \qquad [48]$$

with $U(t_0^+) = R I_0 \bar{t}_0^{\alpha} / \Gamma_{1+\alpha}$, $\bar{t}_0 = t_0/\tau$, and C the linear capacitance, Eq. (32). We thus note, from the evolution of both the fractional exponent (Fig. S8) and the GCD capacitance, that the maximum energy storage is achieved as $I_0 \to 1$, and hence $\alpha \to 1$:

$$\lim_{I_0 \to 0} E_{\text{tot}}^{\text{GCD}} = \lim_{\alpha \to 1} E_C^{\text{GCD}} = \frac{1}{2} C_0 U(t_0^+)^2 \qquad [49]$$

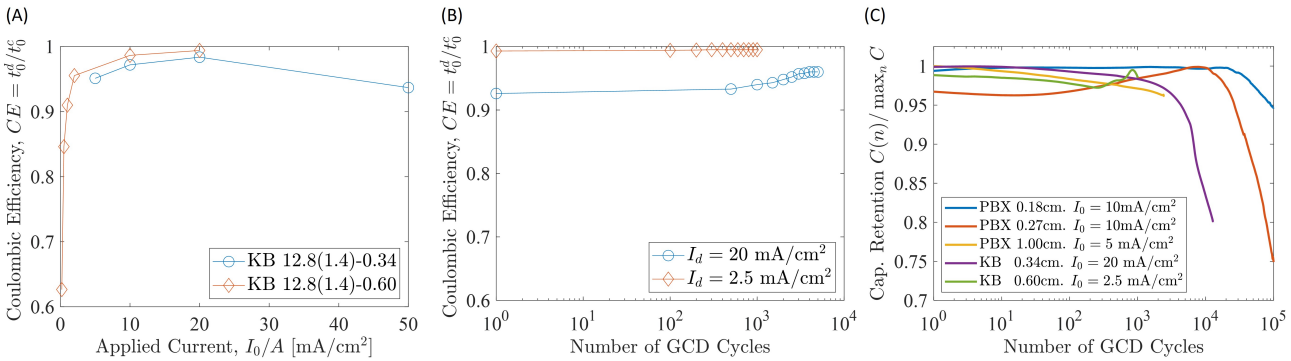

Fig. S9. Coulombic Efficiency (CE) and Capacitance Retention: (A.) Coulombic Efficiency in function of applied current in GCD-test; and (B.) Cyclic Coulombic Efficiency for two electrodes (KB 12.8 (1.4) - 0.34 and KB 12.8 (1.4) - 0.60). (C.) Cyclic Capacitance Retainment, $C(n)/\max_n C(n)$, for a selected number of tested electrodes.

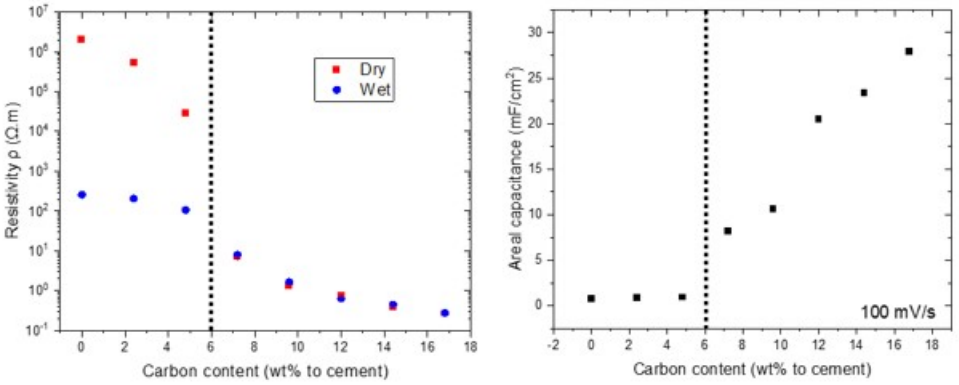

Fig. S10. Nano Carbon Black Threshold Concentration for [left] resistivity (i.e. electron conductivity), and [right] (integer) capacitance (i.e. energy storage) for a PBX doped carbon-cement electrode sample prepared at a water-to-cement ratio of 0.6, and an electrode thickness of 0.25 cm at various nCB concentrations.

where C_0 corresponds to the asymptotic capacitance value as $I_0 \to 0$.

We proceed in a similar fashion for the CV-test. For the charge phase,

$$E_{\text{tot}}^{\text{CV}} = t_0 \frac{U_0^2}{R} \int_0^1 \overline{I}^2 \mathrm{d}\overline{U} + E_C^{\text{CV}}; \qquad E_C^{\text{CV}} = C\bar{t}_0 U_0^2 \int_0^1 \overline{I}\,\overline{U}_C \mathrm{d}\overline{U} \tag{50}$$

Finally, if we evaluate the integrals using Eqn. [26] and [16], at its limit, $\bar{t}_0 \to \infty$ (corresponding to a zero-scan rate), we obtain:

$$\lim_{t_0\to\infty} E_{\text{tot}}^{\text{CV}} = \lim_{\bar{t}_0\to\infty} E_C^{\text{CV}} = CU_0^2 \lim_{\bar{t}_0\to\infty} \frac{(\bar{t}_0 - 2)\exp(\bar{t}_0) + \bar{t}_0 + 2}{2\bar{t}_0(\exp(\bar{t}_0) + 1))} = \frac{1}{2} C_0 U_0^2 \tag{51}$$

The combination of Eq. [49] and Eq. [51] is Eq. [6] in the main text (where we dropped the subscript 'tot'); and proves that the rate-independent capacitance C_0 characterizes the maximum energy storage of the electrodes. It is independent of the testing condition, ion conductivity, and so on. It is why GCD and CV measurements converge as shown in the main text (Fig. 2.D-1 and Fig. 2.D-2).

The values of C_0 for our electrodes are listed in the last column of Table S4.

F. Discussion and Additional Experimental Results of Capacitance Measurements: nCB-Threshold Values. Effect of Aging on Capacitance Measurements. For a selected number of electrode samples we carried out CV-based capacitance measurements to investigate the capacitance at various nCB concentrations. Sample results are shown in Fig. S10, where we display the integral capacitance, Eq. (24), vs. the nCB-concentration (by carbon mass vs. cement mass) for PBX-doped carbon-cement electrodes, prepared at a water-to-cement ratio of 0.6, and an electrode thickness of 0.25 cm. The results demonstrate that the nCB percolation threshold occurs at ca. 6-7% (by carbon mass vs. cement mass). Once the nCB concentration reaches ca. 7%, the capacitance exhibits an (almost) linear increase with the carbon content. This capacitance threshold is comparable to the electrical conductivity threshold. The electrical conductivity threshold of carbon-cement composites was discussed in a previous study (1). In the present study, we selected samples with carbon content beyond the percolation threshold in order to maximize their energy storage potential and identify related texture effects.

A second point we addressed is the influence of material aging on capacitance measurements, by carrying out CV-measurements at an age of 1 month and 30 months, to assess the potential changes in energy storage capacity due to changes in texture parameters over time. The sample result shown for electrode sample PBX 22.4 (0.8) - 0.26 cm in Figure S11 demonstrates that the CV-curves are (almost) not affected by the age of the sample. These results demonstrate that once the main hydration processes are completed (after 28 days of hydration) any additional ongoing hydration does not significantly influence the energy storage potential of our cement-carbon composites. Otherwise said, the texture of the percolated nCB network is stable, and the hydration porosity changes no more.

G. Discussion of Limitation of the Model-Based Approach. The limitations of our modeling approach relate to the assumption of a constant resistance, R, over the testing time. This is a rough estimate for the actual resistivity of the electrolyte which has been shown to change both in space and time (34, 35). On the other hand, to the best of our knowledge, our model-based approach is an improvement of the current best practice of determining the electrode material's performance (see e.g. Ref. (33), Tab. 4) in that it provides a means to obtain one converged capacitance value, C_0, from two different test conditions (here GCD and CV). It is for this reason that we consider C_0 as an intrinsic electrode property characterizing the maximum energy storage.

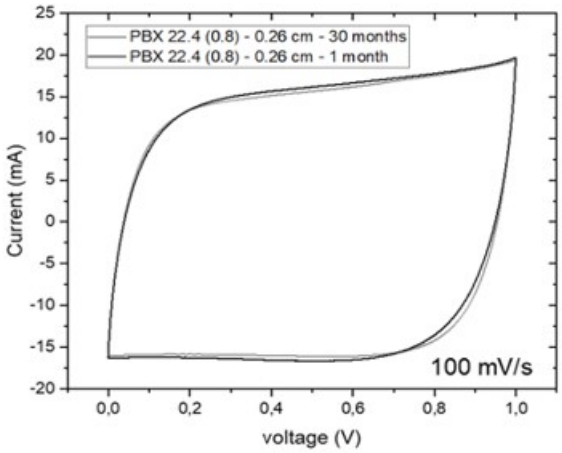

Fig. S11. CV curve at scan rate 100 mV/s at different hydration times (1 month and 30 months) for sample PBX 22.4 at w/c=0.8.

4. Dimensional Analysis and Scaling

This section provides details of the dimensional analysis in the main text, which is the cornerstone of the scaling argument of our paper. We first present the dimensional analysis of the rate-independent capacitance, before turning to the the scaling of high-rate capability of our supercapacitors.

A. Dimensional Analysis of Rate-Independent Capacitance. We experimentally derived a rate-independent capacitance of our electrodes, as the capacitance representative of the maximum energy storage (see Eq. [45]). From an energy storage point-of-view, we consider that the surface of the carbon black is entirely surrounded by an oppositely charged surface layer of ions. Since this 'rate-independent' state does not involve time, the only dependent variables that may affect the capacitance are geometric variables (electrode area A, electrode thickness d), the mass of carbon black in the electrodes, $\phi_C \rho_C$; the specific surface of the carbon black, i.e. S_{BET}, and the aerial capacitance of a carbon black unit surface, ϵ_{nCB}. We are thus interested in the dimensional analysis of the following relationship:

$$C_0 = f(d, A, \phi_C \rho_C, S_{\mathrm{BET}}, \epsilon_{\mathrm{nCB}}) \qquad [52]$$

We consider an $LMTI$ base dimension system, in which any physical quantity is defined by a dimension function:

$$[Q_i] = L^a M^b T^c I^d \qquad [53]$$

Hence, applied to Eq. [52], we have $[C_0] = L^{-2}M^{-1}T^4I^2$, $[d] = [A]^{1/2} = L$, $[\phi_C \rho_C] = L^{-3}M$, $[S_{\mathrm{BET}}] = L^2M^{-1}$, and $[\epsilon_{\mathrm{nCB}}] = L^{-4}M^{-1}T^4I^2$. We summarize the dimension function in form of the exponent matrix of dimension:

$$\begin{array}{c} \\ L \\ M \\ T \\ I \end{array} \begin{array}{c} \begin{array}{cccccc} [C_0] & [\epsilon_{\mathrm{nCB}}] & [d] & [A] & [\phi_C \rho_C] & [S_{\mathrm{BET}}] \end{array} \\ \begin{bmatrix} -2 & -4 & 1 & 2 & -3 & 2 \\ -1 & -1 & 0 & 0 & 1 & -1 \\ 4 & 4 & 0 & 0 & 0 & 0 \\ 2 & 2 & 0 & 0 & 0 & 0 \end{bmatrix} \end{array} \qquad [54]$$

The rank of the matrix is $k = 3$, which means that dimensional analysis (or more specifically the Pi-Theorem (36)) permits us to reduce the dimensional relation (52) between 6 dimensional variables to a relation between $6 - k = 3$ dimensionless invariants; for instance:

$$\frac{C_0}{\epsilon_{\mathrm{nCB}}\, d\, A\, \phi_C \rho_C S_{\mathrm{BET}}} = \mathcal{F}_\pi \left(\frac{d^2}{A}, \phi_C \rho_C S_{\mathrm{BET}}\, d \right) \qquad [55]$$

We test this functional relation using our experimental data (i.e. Tab. S1, S2, and S4), to find out that the dimensional function on the right-hand-side of Eq. [55] is a constant, $\mathcal{F}_\pi = \mathrm{const}$ (see Fig. 3.A in main text). Setting the constant to one, provides the scaling relation, Eq. [7], in the main text.

B. Scaling of Rate Capability. The scaling of the rate-independent capacitance provides an effective means to investigate the parameters governing the rate capability in a dimensionless form, $C(u)/C_0$ (see Fig. 2.E in main text). From the point of view of dimensionless analysis, the dimensionless nature of $C(u)/C_0$ requires that any relation between $C(u)/C_0$ and geometric or electrochemical parameters be dimensionless as well. Motivated by earlier derivations of the spatial and temporal resolution of

ion diffusion, dissociation, solvation and charge storage (34, 35), it is natural to assume that the rate-sensitivity of the capacity measurements are due to the time scale of ion diffusion. From the point of view of dimensional analysis, this means that the scan rate u should scale linearly with a reference scan rate u_0; hence:

$$\frac{C(u)}{C_0} = \mathcal{G}_\pi\left(\xi = \frac{u}{u_0}\right) \quad [56]$$

Given the assumed diffusion control, we scale time t_0 in $u = U_0/t_0$ with the diffusion time, $t_0 = d^2/D$, where D is the diffusivity. In return, the ion diffusivity of a heterogeneous material is affected by the porosity ϕ and the tortuosity $\mathcal{T}$, since $D = \phi D_0/\mathcal{T}$ [see, for instance, (37)]. We now make use of the results of our texture analysis, which revealed that the access to the nanocarbon network, as defined by the specific surface $\phi_C \rho_C S_{\text{BET}}$ is mediated by the specific texture surface of nano carbon black, s_{LD} and s_{HD} (see Fig. 1.F in main text). It is thus natural to consider the ratio of the these specific surfaces as a means to quantify the geometric tortuosity:

$$\mathcal{T} \sim \frac{s_{LD}}{\phi_C \rho_C S_{\text{BET}}} \quad [57]$$

These considerations allow us to scale time t_0 in a dimensionless form:

$$\xi = \frac{d^2}{t_0\, \phi D_0}\mathcal{T} = \frac{d^2\, \phi_C \rho_C S_{\text{BET}}}{s_{LD}\, t_0\, \gamma D_0}\left(\frac{W}{C}\right)^{-3} \quad [58]$$

where the last term, $(W/C)^{-3}$ considers the fact that the hydration porosity, ϕ, and the pores-pace tortuosity are governed by the water-to-cement ratio, W/C (38, 39). The strength and limitation of dimensional analysis is that it provides only scaling relations of physical parameters. The successful scaling of the rate dependence of capacitance is displayed in Fig. 3.B in main text, in which we show that the experimental values of all electrodes tested at different scan rates collapse onto a single master curve. On the other hand, dimensional analysis cannot provide an absolute value for the involved quantities, such as the self-diffusivity, D_0; which is taken into account in our experimentally supported dimensional analysis approach by factor γ in Eq. [58].

Acknowledgment:. This work was supported by the MIT Concrete Sustainability Hub with sponsorship provided by the Concrete Advancement Foundation.

A. APPENDIX

A. Fractional Derivatives. We here consider the Caputo fractional derivative:

$$\frac{\mathrm{d}^\alpha f(t)}{\mathrm{d}t^\alpha} = \frac{1}{\Gamma(1-\alpha)}\int_0^t (t-t')^{-\alpha}\frac{\mathrm{d}f(t')}{\mathrm{d}t'}\mathrm{d}t' \quad [59]$$

for $0 < \alpha < 1$. In contrast to Riemann-Liouville definition of the fractional derivative (used in the fractional capacitance model in Ref. (40)), the Caputo derivative of a constant (say $f(t) = f_0$) is zero:

$$\frac{\mathrm{d}^\alpha f_0}{\mathrm{d}t^\alpha} = 0 \quad [60]$$

The Laplace transform of Eq. (59) reads:

$$\mathscr{L}\left[\frac{\mathrm{d}^\alpha f(t)}{\mathrm{d}t^\alpha}(t)\right](s) = s^\alpha \widehat{f}(s) - s^{\alpha-1} f(0) \quad [61]$$

where $\widehat{f}(s) = \mathscr{L}[f(t)](s)$ stands for the Laplace transform of function $f(t)$, and $f(0) = f(t=0)$ is the initial value of function $f(t)$ at time $t = 0$.

B. Some relevant Laplace Transforms. The Laplace transform of a power function reads:

$$\mathscr{L}(t^\alpha) = \int_0^\infty e^{-st} t^\alpha \mathrm{d}t = \frac{\Gamma(1+\alpha)}{s^{1+\alpha}} \quad [62]$$

for $\alpha > -1$ and $s > 0$. For this calculation, substitute $u := st$ to obtain:

$$\int_0^\infty e^{-st} t^\alpha \mathrm{d}t = \frac{1}{s^{\alpha+1}}\int_0^\infty u^{(\alpha+1)-1} e^{-u}\mathrm{d}u \quad [63]$$

with the integral being identified as the definition of the Gamma function:

$$\Gamma(x) = \int_0^\infty u^{x-1} e^{-u}\mathrm{d}u \quad [64]$$

References

1. NA Soliman, N Chanut, V Deman, Z Lallas, FJ Ulm, Electric energy dissipation and electric tortuosity in electron conductive cement-based materials. *Phys. Rev. Mater.* **4**, 125401 (2020).
2. Cabot Corp., Safety data sheet pbx-55 carbon black, https://www.cabotcorp.com (Revised Version (29-Jan 2018)).
3. Cabot Corp., Vulcan xc72 carbon black, product sheet, https://www.cabotcorp.com (retrieved 12/31/2022).
4. Nouryon Corp., Ketjenblack ec-600jd, electroconductive carbon black, product sheet, https://www.nouryon.com (accessed 12/31/2022).
5. J Jagiello, C Ania, JB Parra, C Cook, Dual gas analysis of microporous carbons using 2d-nldft heterogeneous surface model and combined adsorption data of n2 and co2. *Carbon* **91**, 330–337 (2015).
6. M Miller, C Bobko, M Vandamme, FJ Ulm, Surface roughness criteria for cement paste nanoindentation. *Cem. Concr. Res.* **38**, 467–476 (2008).
7. WC Oliver, GM Pharr, An improved technique for determining hardness and elastic modulus using load and displacement sensing indentation experiments. *J. materials research* **7**, 1564–1583 (1992).
8. B Pichler, et al., Effect of gel–space ratio and microstructure on strength of hydrating cementitious materials: An engineering micromechanics approach. *Cem. Concr. Res.* **45**, 55–68 (2013).
9. F Georget, W Wilson, KL Scrivener, edxia: Microstructure characterisation from quantified sem-eds hypermaps. *Cem. Concr. Res.* **141**, 106327 (2021).
10. HC Loh, HJ Kim, FJ Ulm, A Masic, Time-space-resolved chemical deconvolution of cementitious colloidal systems using raman spectroscopy. *Langmuir* **37**, 7019–7031 (2021).
11. F Tuinstra, JL Koenig, Raman spectrum of graphite. *The J. chemical physics* **53**, 1126–1130 (1970).
12. M Pawlyta, JN Rouzaud, S Duber, Raman microspectroscopy characterization of carbon blacks: Spectral analysis and structural information. *Carbon* **84**, 479–490 (2015).
13. MJ Matthews, MA Pimenta, G Dresselhaus, M Dresselhaus, M Endo, Origin of dispersive effects of the raman d band in carbon materials. *Phys. Rev. B* **59**, R6585 (1999).
14. L Bokobza, JL Bruneel, M Couzi, Raman spectra of carbon-based materials from graphite to carbon black and of some silicone composites. *J. Carbon Res.* **1**, 77–94 (2015).
15. DS Knight, WB White, Characterization of diamond films by raman spectroscopy. *J. Mater. Res.* **4**, 385–393 (1989).
16. A Cuesta, P Dhamelincourt, J Laureyns, A Martinez-Alonso, JD Tascón, Raman microprobe studies on carbon materials. *Carbon* **32**, 1523–1532 (1994).
17. F Sharif, et al., Synthesis of a high-temperature stable electrochemically exfoliated graphene. *Carbon* **157**, 681–692 (2020).
18. FJ Ulm, et al., Statistical indentation techniques for hydrated nanocomposites: concrete, bone, and shale. *J. Am. Ceram. Soc.* **90**, 2677–2692 (2007).
19. S Torquato, H Haslach Jr, Random heterogeneous materials: microstructure and macroscopic properties. *Appl. Mech. Rev.* **55**, B62–B63 (2002).
20. S Torquato, JD Beasley, YC Chiew, Two-point cluster function for continuum percolation. *The J. Chem. Phys.* **88**, 6540–6547 (1988).
21. P Smith, S Torquato, Computer simulation results for the two-point probability function of composite media. *J. Comput. Phys.* **76**, 176–191 (1988).
22. C Yeong, S Torquato, Reconstructing random media. *Phys. Rev. E* **57**, 495 (1998).
23. A Cecen, T Fast, S Kalidindi, Versatile algorithms for the computation of 2-point spatial correlations in quantifying material structure. *Integr Mater Manuf Innov* **5**, 1–15 (2016).
24. S Benito, G Egels, A Hartmaier, S Weber, Statistical characterization of segregation-driven inhomogeneities in metallic microstructures employing fast first-order variograms. *Mater. Today Commun.* **34**, 105016 (2023).
25. S Benito, Matlab Central File Exchange: autocorr2 - two-point autocorrelation (2023).
26. X Jin, J Lu, Simplified methods for determining the ionic resistance in a porous electrode using linear voltammetry. *J. Power Sources* **93**, 8–13 (2001).
27. L Da Silva, L De Faria, J Boodts, Determination of the morphology factor of oxide layers. *Electrochimica Acta* **47**, 395–403 (2001).
28. S Roldán, et al., An approach to classification and capacitance expressions in electrochemical capacitors technology. *Phys. Chem. Chem. Phys.* **17**, 1084–1092 (2015).
29. LM Da Silva, et al., Reviewing the fundamentals of supercapacitors and the difficulties involving the analysis of the electrochemical findings obtained for porous electrode materials. *Energy Storage Mater.* **27**, 555–590 (2020).
30. R Christensen, *Theory of Viscoelasticity. An Introduction.* (Academic Press), 2nd edition, (1982).
31. H Schiessel, R Metzler, A Blumen, TF Nonnenmacher, Generalized viscoelastic models: their fractional equations with solutions. *J. Phys. A: Math. Gen.* **28**, 6567 (1995).
32. WG Nunes, et al., Nickel oxide nanoparticles supported onto oriented multi-walled carbon nanotube as electrodes for electrochemical capacitors. *Electrochimica Acta* **298**, 468–483 (2019).
33. MD Stoller, RS Ruoff, Best practice methods for determining an electrode material's performance for ultracapacitors. *Energy Environ. Sci.* **3**, 1294–1301 (2010).
34. PM Biesheuvel, MZ Bazant, Nonlinear dynamics of capacitive charging and desalination by porous electrodes. *Phys. Rev. E* **81**, 031502 (2010).

35. PM Biesheuvel, Y Fu, MZ Bazant, Diffuse charge and faradaic reactions in porous electrodes. *Phys. Rev. E* **83**, 061507 (2011).
36. G Barenblatt, *Scaling*, Cambridge Texts in Applied Mathematics. (Cambridge University Press), (2003).
37. L Dormieux, D Kondo, FJ Ulm, *Microporomechanics*. (J. Wiley and Sons), (2006).
38. TC Powers, TL Brownyard, Studies of the physical properties of hardened portland cement paste. *Am. Concr. Inst. J. Proc.* **43**, 249–336 (1946).
39. P Pivonka, C Hellmich, D Smith, Microscopic effects on chloride diffusivity of cement pastes—a scale-transition analysis. *Cem. Concr. Res.* **34**, 2251–2260 (2004).
40. A Allagui, ME Fouda, Inverse problem of reconstructing the capacitance of electric double-layer capacitors. *Electrochimica Acta* **390**, 138848 (2021).